Simulation of a Picosecond TOF Device

Shreyas Bhat, Timothy Credo, Henry Frisch
Enrico Fermi Institute, University of Chicago

Abstract

In this paper we describe continuing simulations of a proposed picosecond time-of-flight (TOF) detector based on a microchannel-plate photomultiplier tube (MCP PMT).[1] The system under consideration consists of a large area (5cm x 5cm) MCP PMT. Incident high energy particles produce Cherenkov light as they travel through the PMT window, which is amplified by a microchannel plate and detected on a multi-anode consisting of equal-time impedance-matched transmission lines. Comprehensive simulations of Cherenkov emission, photoelectron production, and signal collection indicate that with the Burle Planacon MCP a 6 picosecond resolution could be achieved. A large area MCP with faster timing characteristics could improve the resolution to 1 picosecond.

1 Introduction

The experimental probing of most of the fundamental problems in particle physics relies on the identification of 'flavor', the quantum numbers that differentiate the 6 kinds of quarks and the three generations of leptons. Investigations of these problems rely on the kinematic reconstruction of events based on the secondary particles observed by a detector; identifying the pions, kaons, and baryons produced in the decay of heavier flavors contributes substantially to our understanding of fundamental physical processes.

The charged hadrons π, K, and p, the predominant types produced in collisions, have very similar interaction characteristics. For momenta above a few GeV most particle detectors can only measure the 3-momentum, and cannot distinguish one hadron from another. The mass can be measured by combining a velocity measurement with the momentum measurement provided by the tracking system. This velocity measurement is the goal of time-of-flight (TOF) systems. Since the secondary particles are typically moving at nearly the speed of light, the time differences between different particles with the same momentum are very small. Figure 1 shows the 1σ separation in flight time for pions, kaons, and protons travelling a 1.5 meter path as a function of momentum. In existing time-of-flight systems, bars of scintillator produce light which bounces over several meters to phototubes at either end. The scintillation process, the long light paths with their consequent variation, and the jitter of conventional photomultipliers all limit the time resolution of these systems.

We aim to extend the identification of particles to higher momenta by designing a time-of-flight system with much better time resolution. We are simulating a TOF detector where particles travel directly through the photodetector itself, generating Cherenkov light which

---

[1]This paper extends previous work by T. Credo, H. Frisch, H. Sanders, R. Schroll, and F. Tang [1]. New in this paper are models of window transmission in the Monte Carlo, simulations using the Burle Planacon anode, a consideration of window thickness and material, simulations of a new summing multianode in HSPICE, and simulations of showering in the magnetic coil.
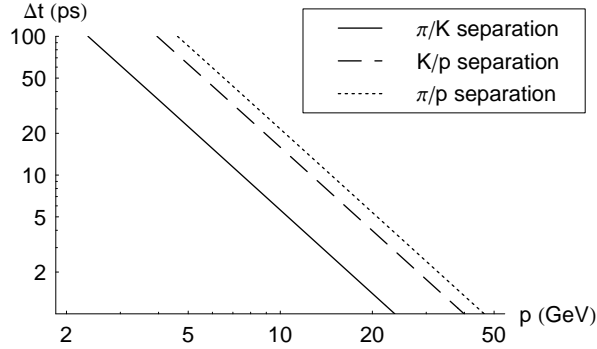
Figure 1: The 1σ separation in time-of-flight over 1.5 meters for pions, kaons, and protons as a function of momentum.

is detected after traversing only a short path length (no bounces). In a detector like CDF or ATLAS, this requires that the collision vertex be surrounded by TOF detectors in a cylindrical array. Particles would be tracked by the tracking system inside the solenoid, and extrapolated to the TOF array to give a precise location of where the particle struck. The particle traversing the window of the photomultiplier tube produces Cherenkov light, which is then converted and amplified by an MCP. This setup eliminates the sources of timing uncertainty associated with a traditional scintillator TOF system.

2   A Picosecond TOF Detector

We intend to show through simulations that a TOF detector in this geometry could achieve timing resolution on the order of one picosecond. In the design under consideration, a particle incident on the front face of a photodetector produces Cherenkov radiation at a characteristic angle as it passes through the window. These photons strike a photocathode, producing photoelectrons with a quantum efficiency depending on wavelength (at most $\sim$25%). As these electrons travel through the pores of the MCP, they produce showers of electrons which land on a multianode that sums these signals at four central collectors. This process is depicted in Figure 2.

   To fully understand the characteristics of this kind of device, we developed comprehensive simulations of the timing characteristics of the phototube and anode. Simulations of Cherenkov emission in the window and the properties of the window, photocathode, and microchannel plate were handled using a ROOT program based on existing phototubes. The locations and times of electron showers arriving at the anode were fed into an HSPICE simulation of a summing multianode to produce pulses characteristic of signals delivered to the electronics. In addition, we examined the effects of window thickness and material on the timing performance of the system, as well as the effect on the system of showering in the magnetic coil.
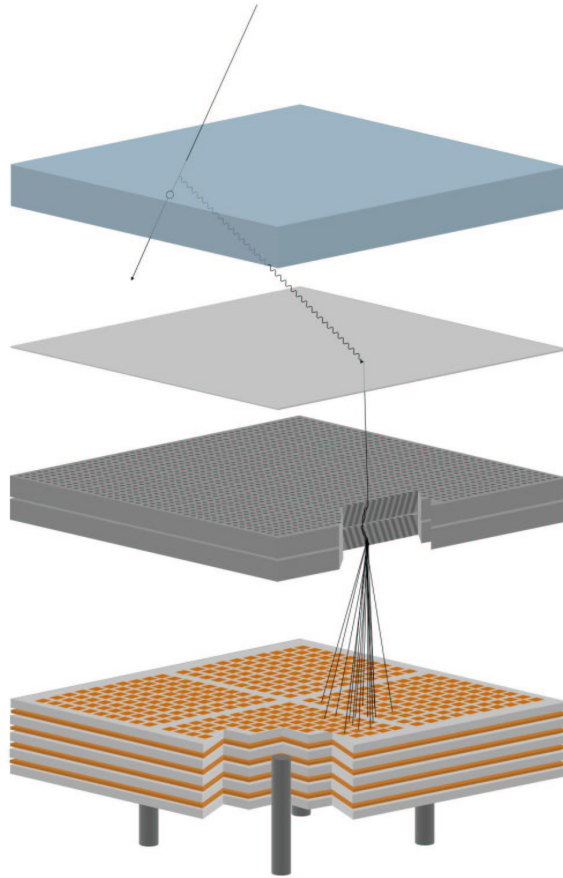
2

Figure 2: As a particle traverses the window of the phototube, it produces Cherenkov photons which strike a photocathode. These signals are amplified by the microchannel-plate and collected on a summing anode.

3   Cherenkov Emission in the Window

In simulation of the window, we examined the effects relevant to the timing performance of the detector. These are:

1. the production of Cherenkov radiation,

2. the probability of absorption in the window,

3. the spread in travel time required for Cherenkov photons to reach the photocathode,

4. and the position of photons striking the photocathode.

In addition we want to examine how the performance of the device is affected by the dimensions and material of the window. We looked at two window materials, fused silica and MgF_2, and a range of window thickness between 1 and 8 millimeters. In general MgF_2 is preferable because it is transparent further into the ultraviolet (where more photons are produced).

Cherenkov radiation is produced by a charged particle in a medium when the velocity of the particle exceeds the velocity of light in that medium [2],[3]. Since the velocity of light in a medium is c/n, where n is the index of refraction, Cherenkov light will be produced whenever $v > c/n$, or using $\beta = v/c$, $\beta n > 1$. This radiation is produced essentially instantaneously. In the limit of an infinite radiating medium, it forms a coherent wavefront in the shape of a cone. The Cherenkov cone has an opening half angle of $\pi/2 - \theta_C$ where

$$\cos\theta_C = \frac{1}{\beta n}.$$

Since in this simulation the thickness of the radiator is on the order of 1000 times the relevant wavelengths, the infinite radiator approximation is valid.

Cherenkov radiation is 'blue'; that is, there is more energy in the shorter wavelengths. The number of photons radiated per wavelength per distance is

$$\frac{\partial^2 N}{\partial x \partial \lambda} = \frac{2\pi Z^2 \alpha}{\lambda^2}\left(1 - \frac{1}{\beta^2 n^2}\right)$$

where Z is the charge of the particle (in multiples of e) and α is the fine structure constant [4],[5]. Since the index of refraction n is a function of wavelength, we approximate $n(\lambda)$ using the Sellmeier equation

$$n^2 - 1 = \frac{B_1 \lambda^2}{\lambda^2 - C_1} + \frac{B_2 \lambda^2}{\lambda^2 - C_2} + \frac{B_3 \lambda^2}{\lambda^2 - C_3}$$

where B_1, B_2, B_3, C_1, C_2, and C_3 are the Sellmeier coefficients for fused silica or MgF_2 [6],[7].

The Monte Carlo algorithm for Cherenkov production in the window works by splitting the radiator into a grid in x, the distance into the radiator, and λ, the wavelength. At each point in the grid $\partial^2 N/\partial x \partial \lambda$ is calculated. After multiplying by $\partial x \partial \lambda$, this is taken to be the probability of photon emission from that location. After randomly deciding whether a photon is produced, the algorithm calculates the position and time that the photon reaches the photocathode and randomly determines, according to the transmission properties of the material [8],[9] (which depend on wavelength), whether the photon is transmitted to the photocathode.

4 The Photocathode and Microchannel Plate

As Cherenkov photons arrive on the photocathode, they produce photoelectrons with a characteristic probability (quantum efficiency) that depends on wavelength. In our simulations, we use a multialkali photocathode, which offers a relatively high quantum efficiency over a wide spectral range. Although the quantum efficiency curve was obtained for a Hamamatsu multialkali photocathode [10], this data is comparable to similar photocathodes produced by other vendors. In the Monte Carlo simulation, the photocathode is modeled by randomly deciding whether each incident photon produced a photoelectron according to the quantum efficiency.

Another factor in the time resolution of the detector is the transit time spread (TTS), or jitter, associated with the MCP itself. The time it takes from the creation of a photoelectron

to the production of a signal will vary slightly from trial to trial. Some of this variation comes from the differences in path length of the first photoelectron, but most arises from uncertainties inherent in the MCP itself. In our simulations, we primarily used the Burle Planacon, with $\sigma_{TTS} = 60$ ps [11], but microchannel plates with smaller pores, lower time spreads, and smaller active areas are available. The TTS is one of the main factors limiting the time resolution of the detector. In our simulation, we approximate the TTS by blurring the times of signals arriving at the anode using a Gaussian with $\sigma = \sigma_{TTS}$.

5 Window Thickness and Material

To understand how the performance of the TOF system depends on the window dimensions and materials, we consider simulations for a range of window thicknesses and for both fused silica and MgF_2. The size of window is limited by the requirement that a particle produce an easily detectable signal and the absorption which begins to dominate around 8 mm. Figure 3 summarizes the timing resolution and signal size for a range of window sizes from 1 mm to 8 mm, calculated from 1000 simulated pulses using the Burle Planacon (with $\sigma_{TTS} = 60$ picoseconds).

Window	RMS Jitter (ps)		Number of Photoelectrons	
Width (mm)	Silica	MgF_2	Silica	MgF_2
1.0	15.31	12.88	16.3 ± 4.0	21.6 ± 4.5
1.5	12.18	10.19	24.2 ± 4.7	32.2 ± 5.4
2.0	10.21	8.74	32.4 ± 5.5	42.6 ± 6.2
2.5	9.27	8.00	40.2 ± 6.2	52.7 ± 7.0
3.0	8.39	7.22	48.2 ± 6.9	63.0 ± 7.5
3.5	7.66	6.84	55.6 ± 7.2	73.4 ± 8.4
4.0	7.12	6.06	63.6 ± 8.0	83.2 ± 8.7
4.5	6.80	5.90	71.1 ± 8.5	93.1 ± 9.5
5.0	6.80	5.71	78.2 ± 8.5	102.6 ± 9.8
5.5	6.38	5.41	85.8 ± 9.2	112.2 ± 10.4
6.0	6.34	5.18	93.0 ± 9.2	122.0 ± 10.5
6.5	5.82	5.04	100.5 ± 9.6	130.9 ± 11.4
7.0	5.71	4.85	109.0 ± 10.4	141.0 ± 11.4
7.5	5.30	4.75	114.8 ± 10.3	148.8 ± 11.4
8.0	5.29	4.59	121.9 ± 10.6	159.4 ± 11.9

Figure 3: A table showing the dependence of the timing accuracy and the signal size on the window thickness, for fused silica and MgF_2. The RMS jitter in picoseconds was measured from the distribution of average signal times (arriving at the anode) for 1000 simulated pulses generated by normally incident particles. The average number of photoelectrons, along with the standard deviation of the distribution, was calculated for the same 1000 pulses.

While it is clear that increasing the window size as much as possible will minimize timing uncertainty, larger window thicknesses translate into a large area of photoelectron showers to

be detected on the anode. As the thickness goes beyond 8 mm, some of nearly every signal will be lost because of the finite size of the anode, which will make the pulse shape vary dramatically from trial to trial. For non-normally incident particles this problem is more severe. A 5 mm window is a good compromise between timing accuracy on the anode and a consistent pulse shape which translates into timing accuracy in the readout electronics.

From this table we can also see that $\sigma_{TTS}/\sqrt{N}$, where N is the number of detected signals, is a good estimate of the timing resolution (to within 10%). Since we expect the timing accuracy to depend primarily on the transit time spread of the microchannel-plate, we compare the results of Table 3 to simulations using an MCP with $\sigma_{TTS} = 10$ ps, consistent with more accurate MCPs with much smaller active areas [12]. For an MgF$_2$ window 5 mm thick, this smaller MCP obtains a timing resolution of 1.0 ps. The distribution of average detection times for the Burle Planacon and for a smaller MCP-PMT are shown in Figure 4 for 5 mm MgF$_2$ windows
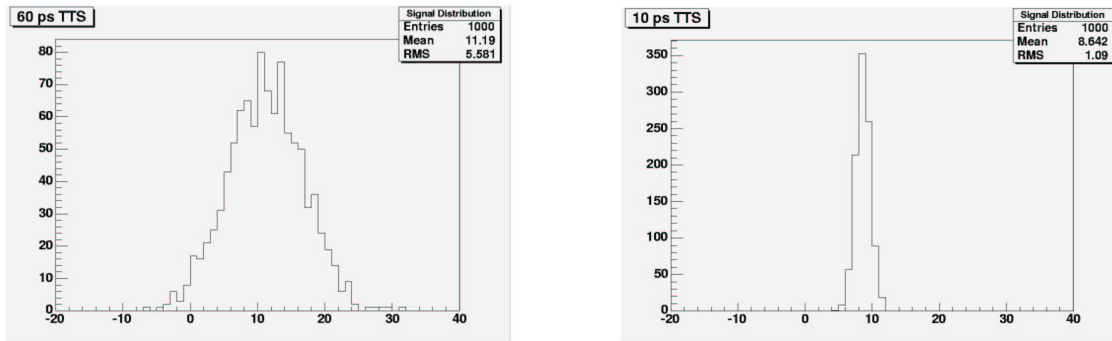

Figure 4: The distribution of detection times for a detector using the Burle Planacon's $\sigma_{TTS} = 60$ ps (left) and a $\sigma_{TTS} = 10$ ps consistent with small area MCPs (right), with a 5 mm MgF$_2$ window. The average times for photoelectron signals arriving on the anode were binned for 1000 simulated pulses.

While these simulations indicate that a timing resolution of ~ 5 ps can be achieved with existing technology, a resolution of ~ 1 ps would require the development of a large area MCP with a transit time spread on the order of 10 picoseconds.

6   Non-normal Incidence

In the previous simulations we have always used particles travelling directly through the device (normally incident). We now consider the effect of non-normal incidence on timing resolution and signal size. Since an incident particle with an angle to the normal, ϕ, greater than about $\pi/4$ will a produce a Cherenkov cone which intersects the photocathode in only a small area, we only consider angles less than $\pi/4$. Figure 5 summarizes the effect of non-normal incidence on timing as a function of the angle ϕ of the incident particle (Appendix A shows the geometry used in calculation of Cherenkov photon position and time for both normal and non-normal incidence).

ϕ (degrees)	σ (ps)	Number of Photoelectrons
0	5.67	102.2 ± 9.6
5	5.68	102.0 ± 10.0
10	5.44	104.3 ± 9.9
15	5.54	105.5 ± 10.2
20	5.46	106.5 ± 9.9
25	5.62	109.1 ± 10.3
30	5.69	109.8 ± 10.4
35	5.53	109.2 ± 10.3
40	5.58	108.8 ± 9.9
45	5.62	107.9 ± 10.1

Figure 5: The effect of non-normal incidence on the timing resolution and signal size is shown as a function of the angle ϕ, for the Burle Planacon with a 5 mm MgF_2 window. The RMS jitter (σ) and average number of photoelectrons were calculated from 1000 simulated pulses for each ϕ.

7   Summing Circuit

Since the speed of light is 300 μm/ps, the resolution of the detector is very sensitive to path length differences as signals travel across the anode to electronics. To avoid the large path length uncertainties inherent in a large area (5 cm x 5 cm) anode, our design uses a 16x16 multianode with each pad routed to a central collector by an equal length transmission line. The four collectors on the back face of the tube deliver the summed signal to electrons. The design for the summing anode board is shown in Figure 6.
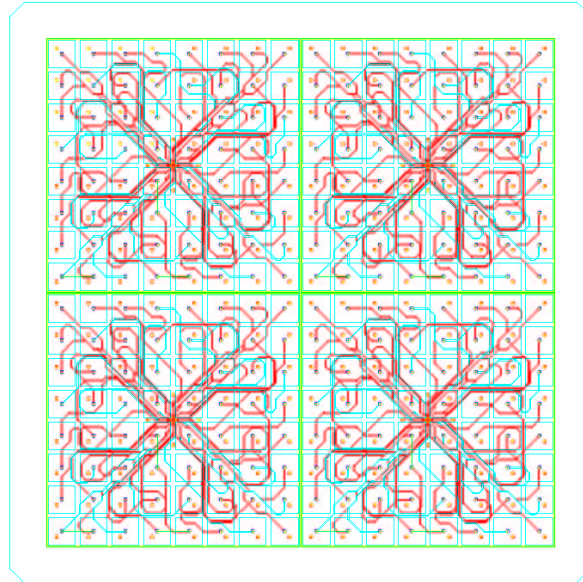

Figure 6: A schematic drawing showing the proposed design for the summing multianode, which shows anode pads and equal length routes.

The transmission lines in the design are all the same length, to within 10 μm, so that the path length uncertainty inside the board is negligible. However, each pad on the surface of the anode is 2700 μm on a side, which is a large enough area to contribute a small uncertainty ($\sigma \approx 1.3$ ps). Since we are averaging this effect out over a large number of electrons in each shower ($\sim 10^6$) and a large number of showers (~ 100), it can be reasonably assumed that it has a very small effect on the time resolution. Since the summing board is a linear system, the jitter in the signal arriving at the anode is (to a reasonable approximation) the time jitter seen in the signal delivered to the electronics.

To understand the shape and the size of the pulse delivered to the electronics, we used a Synopsis HSPICE simulation of the anode board using electrical properties calculated in Mentor Graphics' HyperLynx. A typical shower produced in a 5 mm MgF_2 window produces a pulse of average height $\sim$0.30 V and average rise time $\sim$100 ps at the collector, when using the Burle Planacon. These simulations used a termination of 50 Ω on each collector and a gain in the MCP of 10^6. Since each set of 64 summed lines did not terminate properly, the pulse bounced through the board and decayed with a time constant $\tau \approx 5.5$ ns. Two images of a sample pulse are shown in Figure 7.
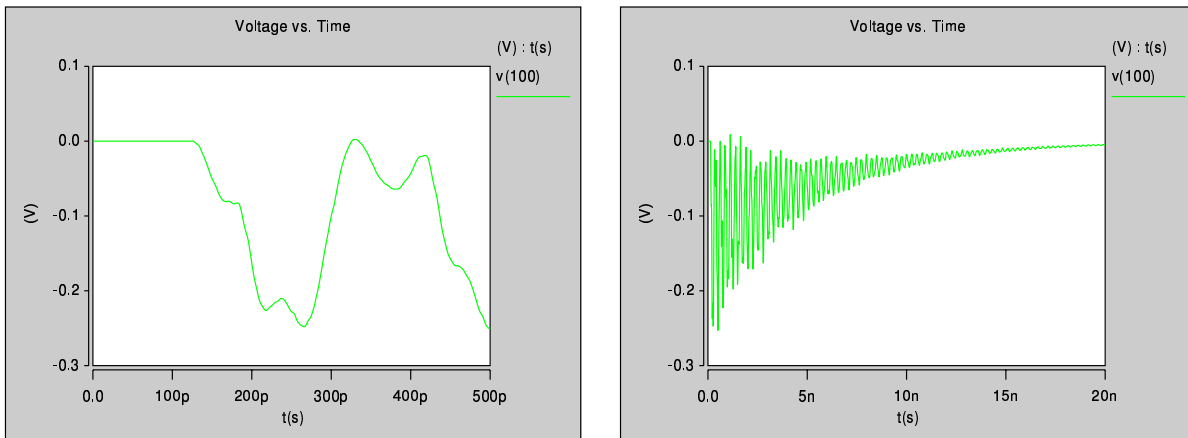

Figure 7: A representative event creates a pulse of -0.23 V with rise time of 80 ps at the collector (left). This pulse bounces through the board for several nanoseconds, as shown by the voltage measured on the collector (right).

The critical part of the pulse seen on the collector is the first rising edge, which will be used to time the pulse by the electronics. Figure 8 shows the rising edge of ten typical pulses seen in a tube using a 5 mm MgF_2 window and the Burle Planacon; Figure 9 shows ten similar simulated pulses for an MCP with $\sigma_{TTS} = 10$ ps. These plots were obtained from HSPICE simulations of the anode combined with ROOT data on the time and position of electron showers. As expected, the timing resolution seen in these two pulses is approximately what we calculated earlier. The pulses produced in a 10 picosecond TTS MCP also had a much smaller pulse width and an average height around 1.3 V. The average rise time was approximately 25 picoseconds.
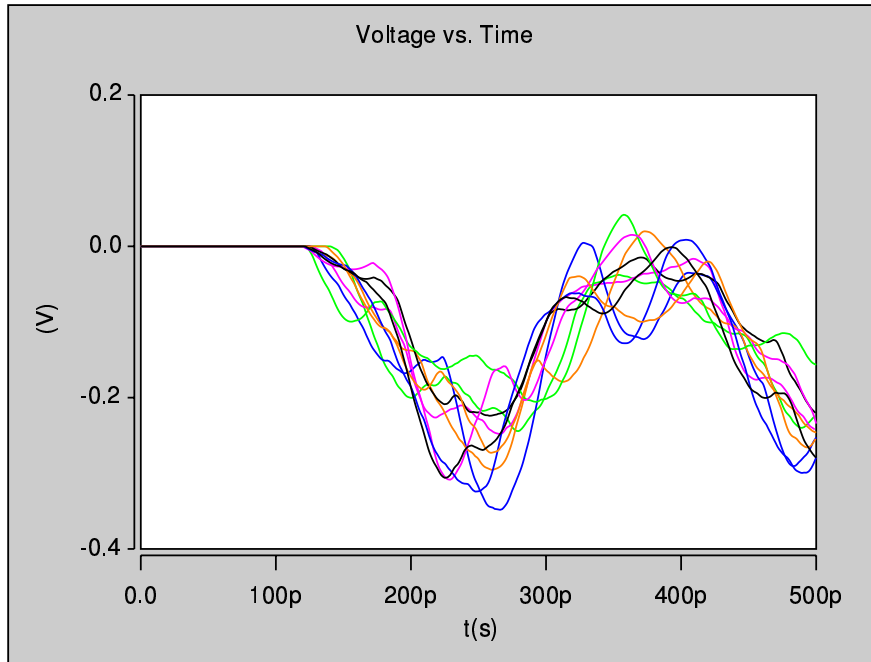
8

Figure 8: A plot of ten simulated pulses on the back of the anode. These voltages were generated using a 5 mm MgF_2 window with normally incident particles and the Burle Planacon MCP. In the HSPICE simulation, the termination on the collector was 50 Ω and the MCP gain was 10^6.
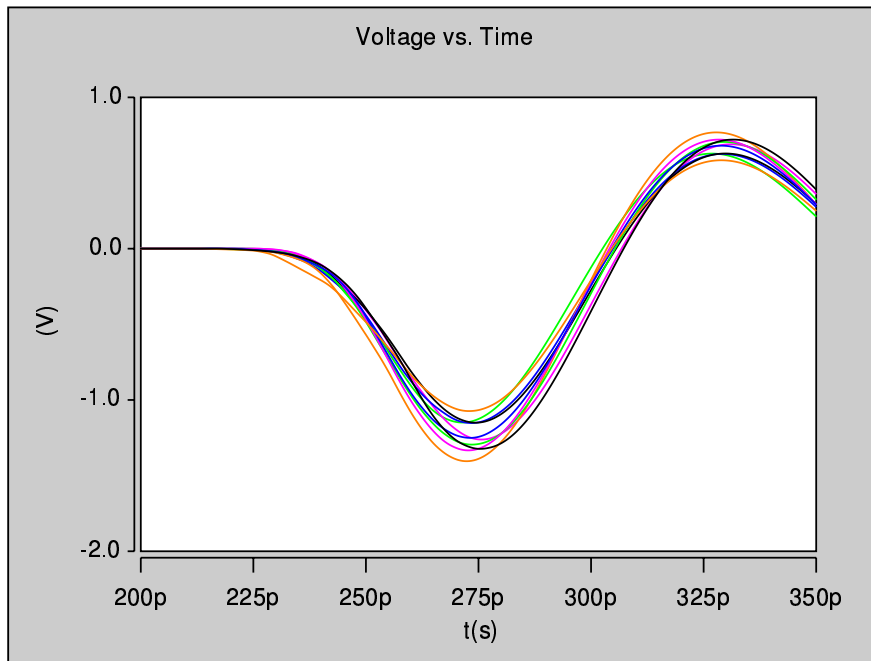

Figure 9: Ten pulses produced in a setup identical to the one in Figure 8 with the Burle Planacon replaced with a micro-channel plate with 10 picosecond TTS.

9

8   Showering in the Coil

An additional minor effect that may impact the timing resolution of the system is showering caused as the particle passes through the solenoid coil. This showering would not have been observed in the tracking system, and thus if a particle produced in a shower reaches the TOF system before the original particle, it may produce a false signal. However, since the tracking system can extrapolate the path of the particle to a specific detector, the only possible uncertainty arises when the original particle and the particles from the shower reach the same detector within a short period of time. Figures 10 and 11 show this.
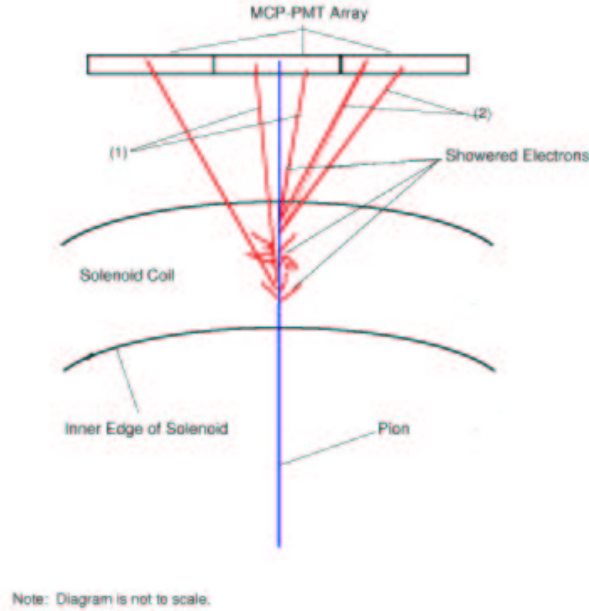

Figure 10: False signals can be created when a pion enters the solenoid coil at normal incidence. The π^+ particle enters the coil from below, as indicated in blue. It creates an electron shower (red), most of which is abosorbed or curls up inside the coil. A few electrons are high enough energy to traverse the coil, and travel to the MCP-PMT array. The false signal occurs when these electrons reach the same detector, as denoted by (1), and within a short period of time of the pion. The electrons that are labeled (2) will not affect the timing because they do not reach the same detector as the pion.

The particles produced will primarily be electrons in the 0.1-100 MeV range, which in the coil's magnetic field have a cyclotron radius

$$r = \frac{p}{qB} \approx p \frac{3\text{mm}}{\text{MeV/c}}.$$

Thus, most of the electrons should curl up over several centimeters in the coil and do not reach the TOF system. Furthermore, since many of the electrons are produced well inside the magnet, most of them will be absorbed by the magnet.
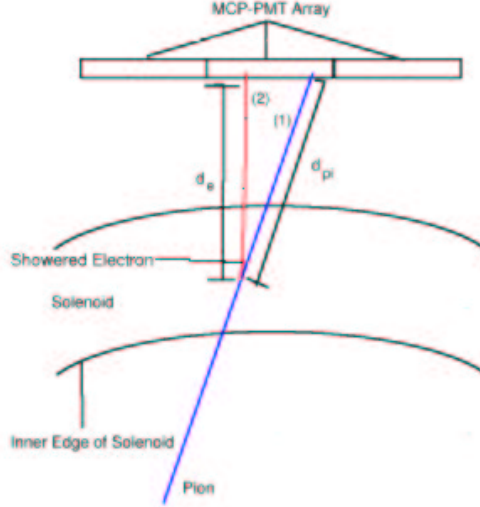
Figure 11: The other case where false signals can also be produced is when the pion is not normally incident on the coil. The pion enters from the lower left, and electrons are showered in the coil as indicated. Some electrons, indicated by (2), can shower so that their distance of travel, d_e, is less than that of the pion (1), d_{pi}. If the electrons are high-energy, this can cause the electron's time of flight to be less than that of the pion, thus causing false signals.

8.1   Geometry

To simulate the effect of showering in the coil on time resolution, we created a cross-sectional model of the coil geometry in GEANT4, released by the GEANT4 collaboration at CERN [13] and observed the showering for 10 GeV π^+ particles. At the point where the pions strike the coil, the coil can be locally modeled by a fixed target. For now, it is described simply as a radiation-length-thick (8.9 cm [14]) slab of aluminum. To this we added a magnetic field that linearly decreases from 12 kGauss at the inner edge to a small residual field (100 Gauss) at the outer edge. Figure 12 shows the geometry from different viewpoints as seen in a 'typical' run, with about 10% of the particles shown here. Table 8.1 lists the geometry of the various components in the simulation. A detailed accounting of the material is given in Ref. [15]; at some point we will update the material to reflect the more detailed situation.

Description	Material	Thickness (cm)	At No (g/mol)	Density (g/cm^3)	Z	X_{rad} (cm)
Coil	Al	8.9	26.98	2.70	13	8.9
Drift	Air	5.0		1.20×10^{-3}		30391.82
	70% N		14.01	1.17×10^{-3}	7	32599.98
	30% O		15.9994	$1.33 \times 10{-3}$	8	25713.98

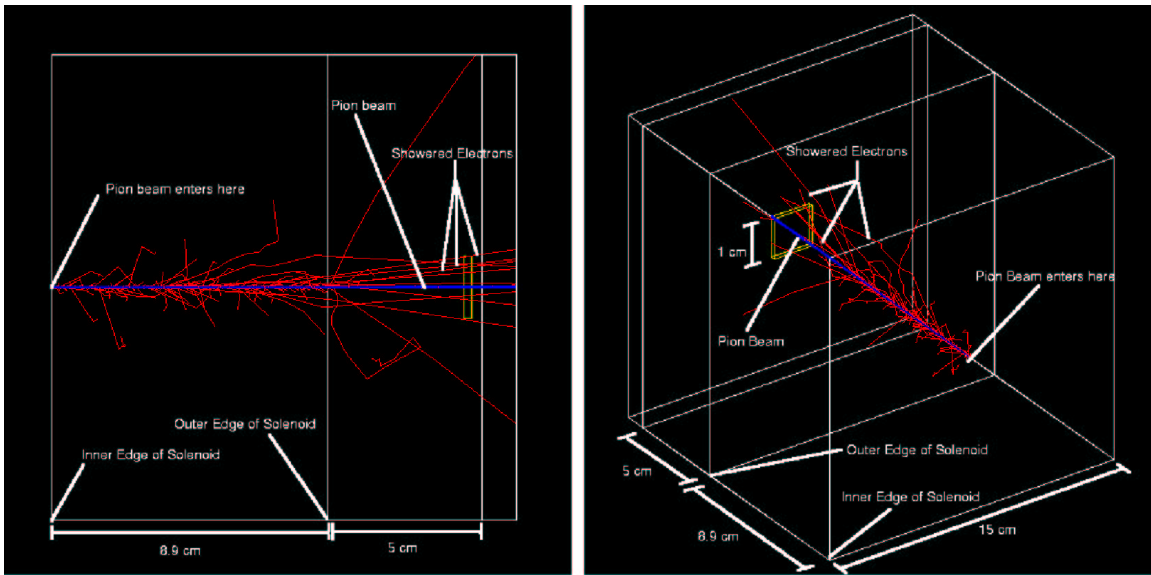Table 1: The components of the simulated CDF Coil and their relevant properties [14].

Figure 12: The geometry of the simulation from two views, with a 'typical' run superposed. In the side view, 10-GeV π^+ particles enter from the left, and in the rotated view, from the lower right. The magnet coil has an internal magnetic field that falls linearly from 12 kG at the inner edge to 100 G at the outer edge as indicated. The π^+ particles are the blue tracks and the showered electrons are the red tracks.

8.2 Technical Details of the Method

Using the example ExampleN02 [16]—a fixed target experiment simulation released by the GEANT4 collaboration—as a basis, we modified the geometry of the target and tracker and changed the magnetic field to accurately represent the magnet and space between it and the TOF system. Information about the various environmental variables and setup conditions used to run GEANT4 is given in Appendix B.

For each run, a 10-GeV charged pion was shot into the coil 1,000 times. At a distance of 5 cm past the outer edge of the magnet, the pion's x-y position and time since its initial release were recorded. The position and time coordinates were also recorded for the showered electrons, and from these, the difference in each coordinate calculated. This experiment was repeated for different incident angles.
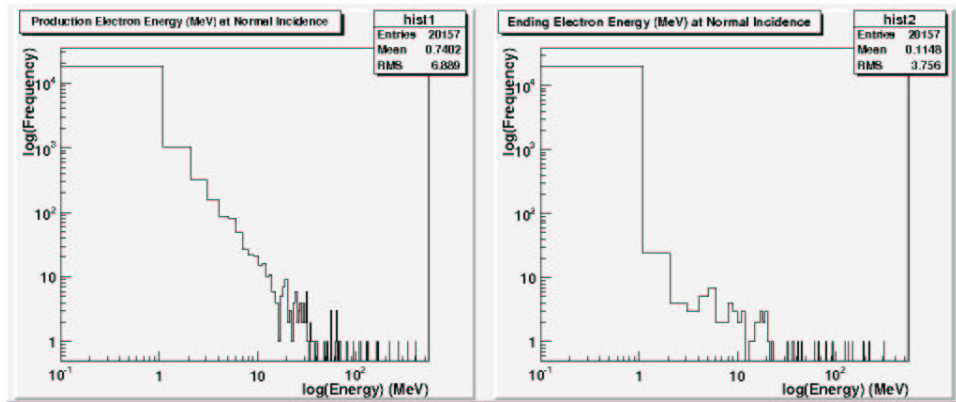
8.3 Results

8.3.1 Normal Incidence

Figure 13: Histograms of initial and final showered energies of normally incident electrons for 1,000 π^+ events. Both plots are on a double-log scale. The range of initial electron energies is from 4.7×10^{-7}–549.0 MeV, and the range of final electron energies is from 0–304 MeV. In both plots, we can see that a significant majority of electrons fall below 1 MeV.

Histograms of electron energies at production and final electron energies are shown in Figure 13. As can be seen, most of the electrons produced have energies well below 1 MeV. Of the original number, 87 electrons are energetic enough to travel 5 cm past the magnet. Figure 14 shows the energy distribution at z = 5 cm past the outer edge of the coil. However, most of this second bunch will either reach this point well after the pions that caused their showering or will strike the PMT array far enough away from the pions. Figure 15 shows the distribution of the spatial and time differences between the pions and their showered electrons.

Since not all of these electrons will affect the timing resolution, we only included the showered electrons that struck both within a 1 in x 1 in square centered at the pion's position and those that struck within 500 ps of the pion. With these cutoffs, the number of electrons that impacted the timing was reduced to 24.
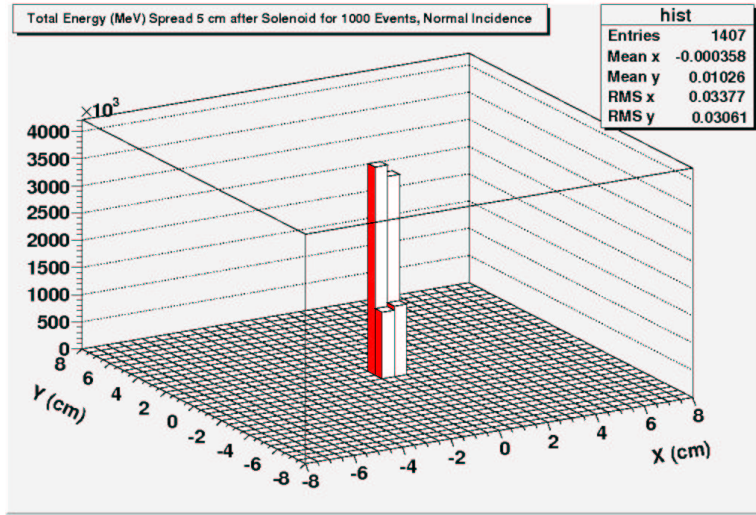
13

Figure 14: The total energy distribution at 5 cm past the coil for 1,000 π^+ events at normal incidence. In this plot, $(x, y) = (0, 0)$ corresponds to the position where a normally incident pion would strike without a magnetic field. As can be seen, the distribution is very concentrated (RMS x and RMS y ≤ 0.034, and there is a slight bias towards the positive $\hat{y}$ direction. We expect this since the magnetic field in the coil is in the $\hat{x}$ direction, and thus the pions travelling in the $\hat{z}$ direction ought to bend in the $\hat{z} \times \hat{x} = \hat{y}$ direction, resulting in slightly more observed energy in the positive y section of the surface.
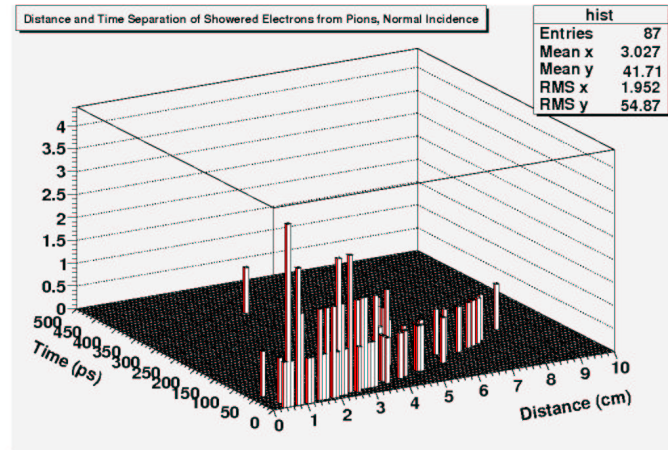

Figure 15: The distribution of the spatial and time differences for pions and showered electrons at normal incidence. The electrons that can produce fake rates can be seen at $(x, y) < (1\,cm, 500\,ps)$.
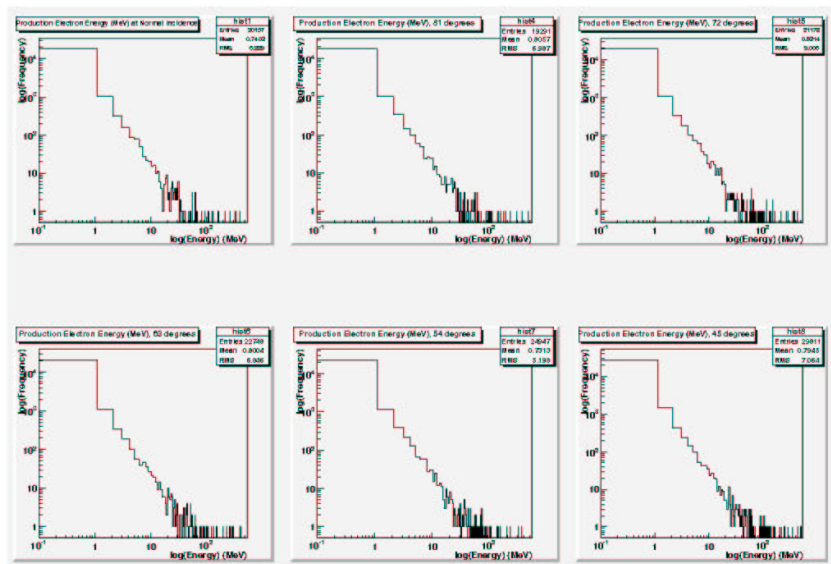
14

8.3.2 Non-normal Incidence

Figure 16: Histograms of showered e^- energies for various incidences for 1,000 π^+ events. The angles used are shown in Table 8.3.2. The top-left histogram is for normal incidence, with angles increasing across the top, and continuing across the bottom, from left to right. Again, it is noteworthy that most electrons' energies fall under 1 MeV.

The simulation described above was also repeated for non-normal incidence. This case is important to investigate because the path length for showered particles to the TOF system could be shorter than that of the original pions, thus leading to shorter recorded times of flight as indicated in Figure 11. We can see in Figure 16 the different distributions of electron energies for different incident angles of the π^+ beam. Figure 17 shows the energy distribution around the incident π^+ beam given different incident angles. Looking at Figure 18 and Table 8.3.2, we can see that at first, as the incidence angle moves away from normal, the pion fake rate initially begins to increase. However, from 18 to 27 degrees, and onwards, we see a decrease in this fake rate. It should be noted that we did not include here results for angles past 45 degrees, since the fake rate is nearly negligible. One possible explanataion is as follows. For a false signal to be produced, the showered electron velocity must be in approximately the same direction as the parent pion. As the incidence angle increases, however, this means that there is more Aluminum in the coil to pass through, leading to a higher probability for absorption. This explanation will be investigated in more depth in the future.

However, given that the largest possible fake rate for pions incident at different angles on the coil appears to be $\sim 5\%$, we do not anticipate electromagnetic showering in the solenoid coil to cause a problem in timing resolution.
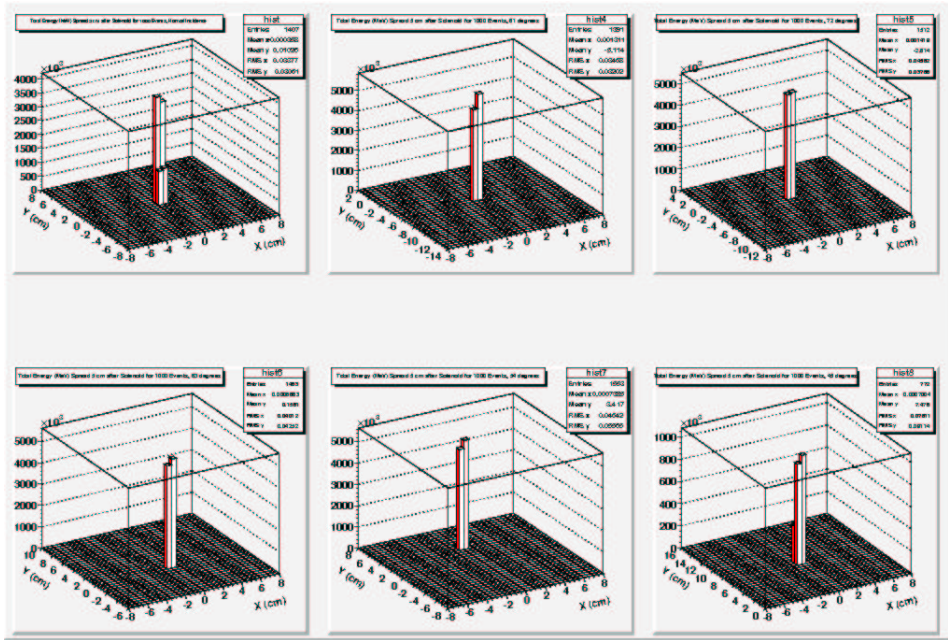
Figure 17: The energy distribution at 5 cm past the coil for 1,000 π^+ events for various incidences. Again, the angles-histogram correspondence is as in Figure 16. Here, the RMS x and RMS y spreads don't change very much, since most electron energies are quite small (see Figure 16). The x-y position of the peaks is arbitrary—only the peak width matters.

Angle of Incidence (°)	Showered Electrons that Reach PMT array	Showered Electrons that Produce False Signal
0	87	24
9	104	46
18	124	49
27	133	40
36	130	30
45	103	18

Table 2: The number of showered electrons that could produce false signals with 1,000 pions incident at different angles.
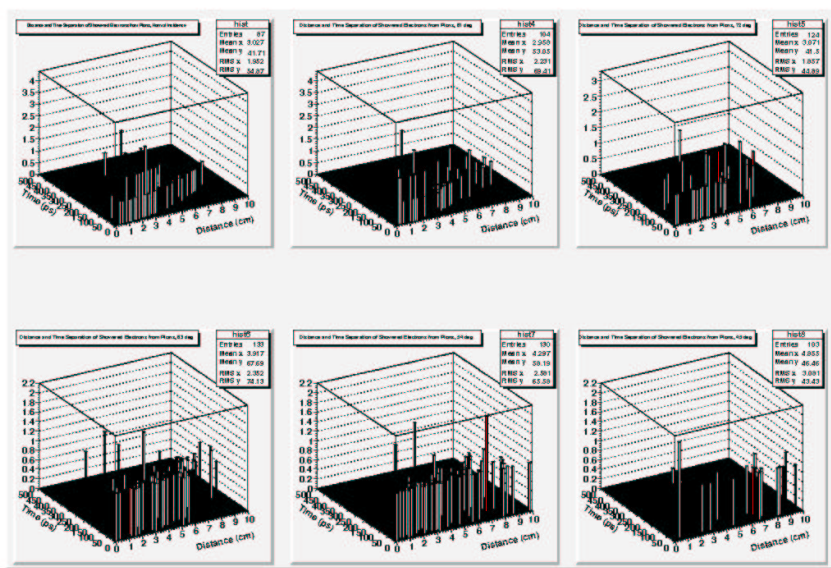
Figure 18: The distributions of the spatial and time differences for pions and showered electrons at various incidences. As before, the electrons that can produce fake rates can be seen at $(x, y) < (1\,cm, 500\,ps)$. The angle-histogram layout is as indicated in the previous figures.

9   Conclusions

Our simulations indicate that fast timing resolution is possible in an array of small (5cm x 5cm) custom MCP PMTs. Several features are worth noting:

1. With the existing Burle Planacon tube and a 5 cm MgF_2 window, we expect to be able to achieve a 6 picosecond timing resolution in the signal delivered to electronics.

2. If a larger area MCP could be developed with the small pore size and fast timing characteristics of existing small area MCPs, the time resolution of this detector could be substantially improved.

3. It appears that the only fundamental limits to the time resolution of a detector in this geometry are the transit time spread of the microchannel-plate and the uncertainty inherent in measuring the electrical pulse produced.

However, there are still several significant issues that are not completely worked out:

1. A charged particle travelling through the detector may create a pulse as it passes through the MCP and the anode which precedes the pulse generated by Cherenkov emission. This phenomenon has been observed in a similar geometry [11].

2. We have assumed in our simulations that the response of an MCP to each photoelectron in a Cherenkov shower is identical to the response to a single photon. This is probably not the case. In general the performance of the MCP under various conditions is not well understood.

3. A time-of-flight system with this resolution requires electronics capable of measuring and digitizing the collected pulse.

4. Implementing a large array of these devices requires a very fast way to synchronize the individual detectors in the system.

We are confident that if these obstacles can be overcome, a TOF system consisting of custom MCP-PMTs could be developed with resolution on the order of one picosecond.

References

[1] H. Frisch, et al, *IEEE NSS 2004 : Conference Record*, N16-83 (2004).

[2] K. Kleinknecht, *Detectors for Particle Radiation, 2nd Edition*, University Press, Cambridge (1998).

[3] W. Leo, Techniques for Nuclear and Particle Physics Experiments, Springer-Verlag, New York (1994).

[4] CDF-II Collaboration, *Nuclear Instruments and Methods* 518, 605-608 (2004).

[5] S. Cabrera, J.P. Fernandez, et al, *Nuclear Instruments and Methods* 484 416-423 (2002).

[6] Union Optic, *Optical Materials* http://www.u-optic.com/material.htm

[7] Corning Incorporated, *HPFS Fused Silica Standard Grade* http://www.corning.com/ semiconductoroptics/products_services/pdf/h0607_hpfs_standard_productsheet.pdf

[8] Red Optronics, *Optical Materials: MgF_2* http://www.redoptronics.com/MgF2-optical-material.html

[9] Edmund Optics, *Technical Specifications: UV Fused Silica Windows* http://www.edmundoptics.com/onlinecatalog/displayproduct.cfm?productID=2076

[10] Hamamatsu Corporation, *2002 Catalog Excerpts: MCP-PMTs*, http://usa.hamamatsu.com/assets/pdf/catsandguides/PMTCAT_special_mcp-pmt.pdf

[11] M. Akatsu, et al, *Nuclear Instruments and Methods* 528, 763-775 (2004).

[12] Hamamatsu Corporation, *2002 Catalog Excerpts: MCP-PMTs* http://usa.hamamatsu.com/assets/pdf/parts_R/R3809U-50.pdf

[13] GEANT4 Collaboration, CERN, *GEANT4 Home Page*, http://geant4.cern.ch/

[14] S. Eidelman et al., *The Review of Particle Physics, 2004*, Phys. Lett. B 592, 1 (2004)

[15] Minsuk Kim, Ray Culbertson, Robert Blair; *CPR Material Counts of CDF Run II*; CDF Note CDF/PUB/CDF/PUBLIC/6101; 8/27/02

[16] GEANT4 Collaboration, CERN, Included in GEANT4 package download. See http://geant4.cern.ch/

[17] D. Elvira., P. Spentzouris, and J. Yarba, *GEANT4 at Fermilab*, http://cepa.fnal.gov/psm/geant4/

A Geometry used in the Monte Carlo

A sketch of the geometry is shown below. Since the results of the any simulation can be rotated and translated, it suffices to consider particles with velocities in the x and z directions, and to make the origin the point on the photocathode which corresponds to where the particle enters the window. In the diagram, i is the iteration number and nx is the total number of iterations along the particles path (using intervals ∂x).
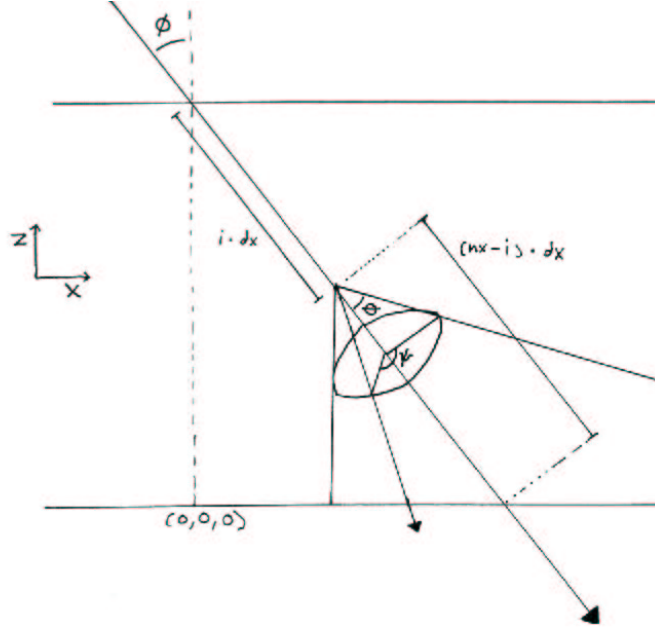
A unit vector in the direction of the particle is clearly $\hat{\mathbf{v}}_{\mathbf{p}} = (\sin\phi, \mathbf{0}, -\cos\phi)$. From the requirement that the path of the photon be at an angle $\cos\theta_C$ to the path of the particle, we can obtain a unit vector in the direction of the photon's path

$$\hat{\mathbf{v}}_\gamma = \cos\theta_{\mathbf{C}}\hat{\mathbf{v}}_{\mathbf{p}} + \sin\theta_{\mathbf{C}}(\cos\psi\cos\phi, \sin\psi, \cos\psi\sin\phi).$$

Note that as expected $\hat{\mathbf{v}}_{\mathbf{p}} \cdot \hat{\mathbf{v}}_\gamma = \cos\theta_{\mathbf{C}}$ since the second term is orthogonal to the particle's path. The angle ψ corresponds to an arbitrary rotation around the particle's path; in the Monte Carlo it will be given a uniform distribution.

Since this vector completely determines the direction of the photon, we can use it to find the intersection of the photon's path with the xy plane. This is the point where the photon strikes the photocathode. The point (x, y) is given by:

$$x = i * \partial x * \sin\phi + (nx - i) * \partial x * \cos\phi \left(\frac{\cos\theta_C \sin\phi + \sin\theta_C \cos\psi \cos\phi}{\cos\theta_C \cos\phi - \sin\theta_C \cos\psi \sin\phi} \right)$$

$$y = (nx - i) * \partial x * \cos\phi \left(\frac{\sin\theta_C \sin\psi}{\cos\theta_C \cos\phi - \sin\theta_C \cos\psi \sin\phi} \right)$$

Since we can now calculate all the relevant distances, we can easily determine the timing information and calculate the probability of absorbtion.

B GEANT4 Setup

GEANT4 is a very powerful simulation toolkit that simulates particle interactions with matter. This appendix outlines the various environmental variables that are necessary set in order to run GEANT4 on a UNIX system. For the purposes of this explanation, the examples of commands are given for csh (i.e. *setenv* as opposed to *export*).

If you are accessing GEANT4 from an outside machine (i.e. ssh), it is crucial for visualization that X-forwarding is enabled. This can be done by adding "-X" or "-Y" before the server name. To access the Open-GL drivers and to use them for rendering visualization, set the following variables:
setenv G4VIS_BUILD_OPENGLX_DRIVER 1
setenv G4VIS_USE_OPENGLX 1

setenv OGLHOME /usr/X11R6
setenv OGLFLAGS "-I$OGLHOME/include"
setenv OGLLIBS "-L/usr/X11R6/lib -lGL -lGLU"

Furthermore, one must set the following environmental variables for GEANT4 to create and run executables properly:
setenv G4WORKDIR ~/G4test
setenv G4TMP $G4WORKDIR/tmp
setenv G4BIN $G4WORKDIR/bin

It is advisable to put these commands in a script that can simply be run at every login, instead of having to run them separately. However, it is important to remember that on some machines, the software has to be setup before setting environmental variables.

Now GEANT4 should run perfectly well!

More information about GEANT4 can be found at the the websites [17] and [13].